Supplementary information

A Novel High-performance All-liquid Formic Acid Redox Fuel Cell: Simultaneously Generating Electricity and Restoring Capacity of Flow Batteries

Dongbo Wei,[a,†] Lyuming Pan,[a,†] Jing Sun,[b,†] Meisheng Han,[a] Manrong Song,[a] Jincong Guo,[a] Qing Zhang,[a] Cailin Xiao,[a] Zheng Li,[a] Yubai Li,[d] Shuaibin Wan,[c] Lin Zeng[a,*], Lei Wei[a,*], Tianshou Zhao[a,*]

[1] *Shenzhen Key Laboratory of Advanced Energy Storage, SUSTech Energy Institute for Carbon Neutrality, Department of Mechanical and Energy Engineering, Southern University of Science and Technology, Shenzhen 518055, China.*

[2] *Department of Mechanical and Aerospace Engineering, The Hong Kong University of Science and Technology, Clear Water Bay, Kowloon, Hong Kong SAR, China.*

[3] *Shenzhen International Center for Industrial and Applied Mathematics, Shenzhen Research Institute of Big Data, Guangdong, China*

[4] *Key Laboratory of Ocean Energy Utilization and Energy Conservation of Ministry of Education, Dalian University of Technology, Dalian 116023, China*

[†] *These authors contributed equally.*

[*] Corresponding author

Email addresses: zengl3@sustech.edu.cn (Lin Zeng), weil@sustech.edu.cn (Lei Wei), zhaots@sustech.edu.cn (Tianshou Zhao),

Notes

Figures

Tables

Supplementary Note 1 The details of LSV tests for ORR and V^{5+} reduction reaction

Linear sweep voltammetry (LSV) tests were conducted using the electrochemical workstation (CHI 760E, China). A three-electrode cell was used to assess the kinetic current densities of the V^{5+} reduction reaction on graphite felt (Liaoning Jingu Carbon Materials Co., Ltd, China) and the oxygen reduction reaction (ORR) on the catalysts. The graphite felt was thermally treated and cut into circular pieces with an area of 0.196 cm^2, serving as the working electrode. A saturated calomel and a platinum mesh were used as reference and counter electrodes, respectively. The V^{5+} reduction reaction was evaluated in a 0.1 M V^{4+} + 3.0 M H_2SO_4 electrolyte, with a voltage sweep from 0.2 to 1.05 V (vs. RHE) at a scan rate of 10 mV s^{-1}. ORR tests on Pt/C were executed in a similar setup, employing a 0.196 cm^2 glassy carbon (GC) electrode as the working substrate. For the test, 2 mg of the catalysts (Pt/C: 40 wt. %) were dispersed in 0.98 mL isopropanol with 20 µL of 5% Nafion (D520, Dupont Inc., USA), ultrasonicated for 60 minutes, and then deposited on the GC electrode to achieve a Pt/C loading of 15 µg cm^{-2}. ORR tests were carried out in 0.1 M $HClO_4$ electrolyte pre-saturated using O_2 for 30 minutes to ensure saturation during the measurements with a voltage sweep from 0.2 to 1.05 V (vs. RHE) at a scan rate of 10 mV s^{-1}. The rotating speed for the ORR tests on the rotating disk electrode was set at 1600 rpm.

Supplementary Note 2 The calculation details of the electrochemical active surface areas (ECSA) of catalysts

ECSA was determined by the desorption peak of two catalysts using the following equation:

$$ECSA\ (m^2\ g^{-1}) = Q\ (\mu C) / 0.21\ (\mu C\ m^{-2}) / M\ (g) \quad (1)$$

Q represents the electric double-layer capacitance current of the electrode, can be considered as the charge amount of the desorption of the adsorbed hydrogen, and M is the mass of loading metal. 0.21 $\mu C\ m^{-2}$ is the hydrogen adsorption charge constant on the Pt surface as a monolayer. The desorption hydrogenated adsorbates peak was obtained from Figure S7. CV curves were recorded in an Ar-saturated 0.5 M H_2SO_4 electrolyte from 0.05 to 1.2 V vs. RHE at a scan rate of 50 mV s^{-1}.

Supplementary Note 3 The calculation details of the Bi coverage

The coverage of Bi atoms on Pt nanoparticles can be calculated as follows: [1]

$$\text{Bi coverage} = (Q_{Pt/C} - Q_{\text{Bi-modified Pt/C}}) / (3Q_{Pt/C}) \quad (2)$$

$Q_{Pt/C}$ is the area (0.471) of the hydrogen adsorption/desorption peaks from 0.05 to ~0.45 V in the CV curve of Pt/C (Figure S7a). $Q_{\text{Bi-modified Pt/C}}$ is the area (0.115) of the hydrogen adsorption/desorption peaks from 0.05 to ~0.45 V in the CV curve of Bi-modified Pt/C (Figure S7b). Thus, the calculated coverage of Bi atoms on Pt nanoparticles is about 0.25.

Supplementary Note 4 The experiment details of in-situ FTIR spectroscopy

Electrochemical in-situ FTIR reflection spectroscopy was performed on a Bruker 70 V FTIR spectrometer equipped with a liquid-nitrogen-cooled MCT-A detector. 10 μL of catalyst ink was transferred on a glass carbon electrode quipped with a specially-made three-electrode thin-layer IR cell configuration, using CaF_2 as the window. It was tested in 0.5 M H_2SO_4 + 0.5 M HCOOH at a scan rate of 2 mV s^{-1} from 0.1 V to 1.1 V, and the in-situ FTIR spectra were collected from 0.1 V to 1.1 V per 0.1 V.

Supplementary Note 5 The details of the Density Functional Theory (DFT) calculation

In this study, spin-polarized DFT calculations were conducted using the Generalized Gradient Approximation (GGA) and Perdew-Burke-Ernzerhof (PBE) formulation.[2, 3] The ionic cores were described using Projected Augmented Wave (PAW) potentials, and valence electrons were accounted for with a plane wave basis set and a kinetic energy cutoff of 450 eV.[4, 5] Van der Waals interactions have been considered using the DFT-D3 method of Grimme.[6, 7] The electronic energy convergence threshold was set at 10^{-5} eV, and geometric optimization was deemed complete when energy changes fell below 0.02 eV $Å^{-1}$. Relaxation utilized a 3×3×1 Gamma-centered grid in the Brillouin zone, with a 15 Å vacuum layer to prevent spurious periodic interactions.

The Gibbs free energy change (ΔG) of each elementary step was computed as the sum of the reaction energy (ΔE), derived from DFT, and the adjustments for zero-point energies (ΔZPE) and entropy (ΔS), following the equation:

$$\Delta G = \Delta E + \Delta ZPE - T\Delta S \quad (3)$$

The adsorption energy (E_{ads}) is calculated as E_{ads} = E(total) - E(slab) - E(CO). E(total) is the total energy of an optimized slab with the CO on it, E(slab) is the energy of a relaxed, clean slab, and E(CO) is the energy of a CO molecule. There are four high-symmetry adsorption sites on the (111) surface of Pt, namely, atop, bridge, face-centered cubic (fcc), and hexagonal-close packed (hcp) site. The effect of Bi doping on Pt was analyzed by comparing the adsorption energies at these sites, as well as the optimal fcc site, with Bi coverage of ~0.25, assessing the changes induced by Bi on CO adsorption energies, as illustrated in Figures S9 and S10.

Supplementary Note 6 The details of 3D multi-physical models

Geometry details

The 3D multi-physical model consists of two flow fields, two electrodes and a membrane with an actual area of 2.0×2.0 cm^2. The geometric structure of the flow field is an interdigitated flow field composed of 1 inlet, 1 outlet, and 10 flow channels. Besides, the depth of the channel is 1.5 mm, and the width is 1.0 mm.

Physical assumptions

The physical assumptions for the model are as follows:

1) The electrolytes are regarded as laminar, incompressible fluid, and isothermal domain.

2) The electrodes are isotropic and uniform, where the catalysts' layer and gas diffusion layer at the negative side are treated as a single porous medium.
3) Ignore all side reactions on the positive sides, including oxygen evolution reactions.
4) Carbon dioxide is considered completely soluble. Thus, the electrolyte is considered a single-phase flow.
5) The influence of gravity is not taken into account.

Governing equations

The laminar fluid flow equation of the incompressible fluid in the main flow channel assumes that the fluids are Newtonian, with a constant density and viscosity. The continuity (mass balance) and Navier–Stokes (momentum balance) equations used to calculate the flow in the flow field: [8]

$$\nabla \cdot \vec{u} = 0 \tag{4}$$

$$\rho(\vec{u} \cdot \nabla\vec{u}) = -\nabla p + \mu\nabla^2\vec{u} \tag{5}$$

where $\vec{u}$, ρ and μ are the velocity, density and viscosity of the electrolyte.

The Brinkman equation reveals the flow within porous electrode: [9]

$$\nabla \cdot \vec{u} = 0 \tag{6}$$

$$\frac{\rho}{\varepsilon^2}(\vec{u} \cdot \nabla\vec{u}) = -\nabla p + \frac{\mu}{\varepsilon}\nabla^2\vec{u} - \frac{\mu}{k}\vec{u} + \beta_F\nabla^2\vec{u} \tag{7}$$

where ε is the porosity of the porous media, p is the pressure, μ is the dynamic viscosity of the electrolyte, and k is the permeability of the porous media. β_F is the Forchheimer drag coefficient, which is ignored in the simulation. Since gravity is also not considered in the model, the volume force acting on the fluid is zero.

The Nernst-Plank equation describes the transfer process of dilute species in porous media. The equation includes diffusion item, migration item, and convection item: [10]

$$\overrightarrow{N_i} = -D_i^{eff}\nabla c_i - \frac{z_i c_i D_i^{eff} F}{RT}\nabla\varphi_i + \vec{u}c_i \tag{8}$$

The conservation of each species can be expressed as: [10]

$$\nabla\overrightarrow{N_i} = S_i = \frac{v_i i_{pos/neg}}{n_i F} \tag{9}$$

where the subscript i represents a certain species, and $\overrightarrow{N_i}$ represents the flux of the species, S_i the species' source term indicates the generation rate due to electrochemical reactions. $c_i$and z_i represent the concentration and charge of a species i, respectively. R is the ideal gas constant, T is the temperature, and F is the Faraday's constant. φ_i is the potential of a species in the liquid phase. The v_i , n_i and $i_{pos/neg}$ denote the stoichiometric coefficient, the number of participating electrons, and the corresponding positive/negative current density.

The effective diffusion coefficient D_i^{eff} can be obtained by Bruggeman's modification: [11]

$$D_i^{eff} = \varepsilon^{\frac{3}{2}} D_i \tag{10}$$

The charge conservation on the positive and negative sides is solved as the following two equations, respectively: [12]

$$\nabla \cdot \overrightarrow{i_{s,pos}} = -\nabla \cdot \overrightarrow{i_{l,pos}} = i_{pos} \tag{11}$$

$$\nabla \cdot \overrightarrow{i_{s,neg}} = -\nabla \cdot \overrightarrow{i_{l,neg}} = i_{neg} \tag{12}$$

where $\vec{i_s}$ and $\vec{i_l}$ are the current densities of the solid and liquid phases, respectively.

The results can also be obtained using the Butler-Volmer equations, where the positive side is determined as:

$$i_{pos} = a_{pos} i_{0,pos} [\exp(\frac{\alpha_{n,c} F \eta_{pos}}{RT}) - \exp(-\frac{\alpha_{n,a} F \eta_{pos}}{RT})] \quad (13)$$

$$i_{0,pos} = F k_{0,pos} c_{V^{4+}}^{\alpha_{p,c}} c_{V^{5+}}^{\alpha_{p,a}} \quad (14)$$

where $i_{0,pos}$ and $k_{0,pos}$ are the exchange current density and reaction rate coefficients on the positive side, respectively. a_{pos} defines the specific surface area for the positive electrode. $\alpha_{p,a}$ and $\alpha_{p,c}$ are the anodic and cathodic charge transfer coefficients, respectively. η_{pos} represents the positive overpotential.

The negative side is determined as follows: [13]

$$i_{neg} = a_{neg} i_{0,neg} (\frac{c_{FA}}{c_{FA,ref}})^{\beta} [\exp(\frac{\alpha_{n,a} F \eta_{neg}}{RT}) - \exp(-\frac{\alpha_{n,c} F \eta_{neg}}{RT})] \quad (15)$$

$$\beta = \begin{cases} 0, c_{FA} > c_{FA,ref} \\ 1, c_{FA} \leq c_{FA,ref} \end{cases} \quad (16)$$

where $i_{0,neg}$ is the exchange current density on the negative side. a_{neg} defines the specific surface area for the negative electrode. $\alpha_{n,a}$ and $\alpha_{n,c}$ are the anodic and cathodic charge transfer coefficients, respectively. η_{neg} represents the negative overpotential.

The 3D model is implemented through commercial software COMSOL Multiphysics, and the parameters involved are defined in **Table S2**.

Supplementary Note 7 Working principle of VRFBs

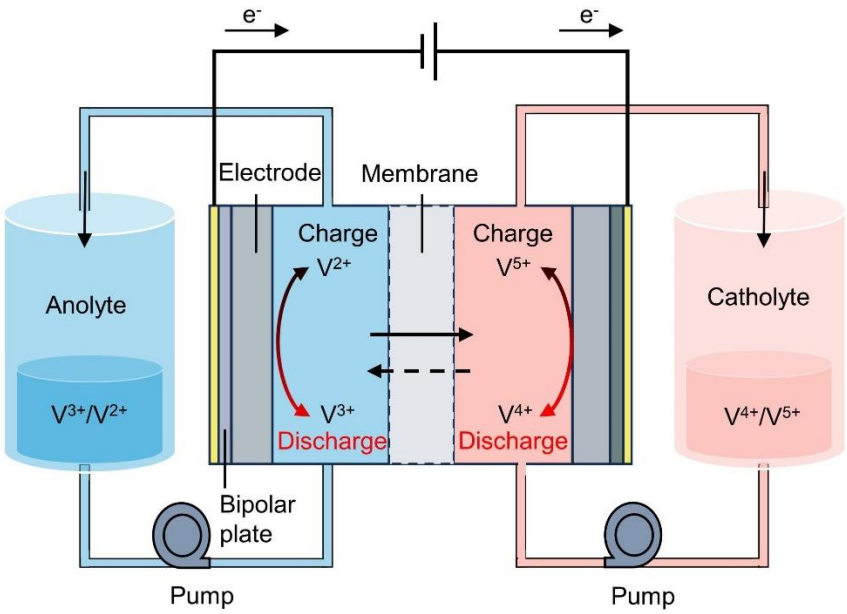

Positive reaction: $V^{4+} \leftrightarrow V^{5+} + e^{-}$ (17)

Negative reaction: $V^{3+} + e^{-} \leftrightarrow V^{2+}$ (18)

Overall reaction: $V^{4+} + V^{3+} \leftrightarrow V^{5+} + V^{2+}$ (19)

Supplementary Note 8 The details on CV and EIS tests of pure V^{4+} electrolyte and discharged catholyte.

CV and EIS tests were conducted using the electrochemical workstation of Chen Hua (CHI 760E, China) to examine the electrochemical properties of pure V^{4+} electrolytes and discharged catholytes. The electrochemical properties of pure V^{4+} electrolyte were examined in a 0.1 M V^{4+} + 3.0 M H_2SO_4 electrolyte solution. The electrochemical properties of the discharged catholyte were evaluated in a 0.1 M discharged catholyte + 3 M H_2SO_4. CV tests were performed with voltage sweep ranging from –0.659 to 0.241 V (vs. RHE) at a scan rate of 20 mV s^{-1}. For the EIS tests,

the tests were performed across a frequency range of 100 kHz to 0.01 Hz with an amplitude of 10 mV at a fixed voltage of 1.141 V (vs. RHE).

Supplementary Note 9 The detailed capacity recovery process for VRFBs

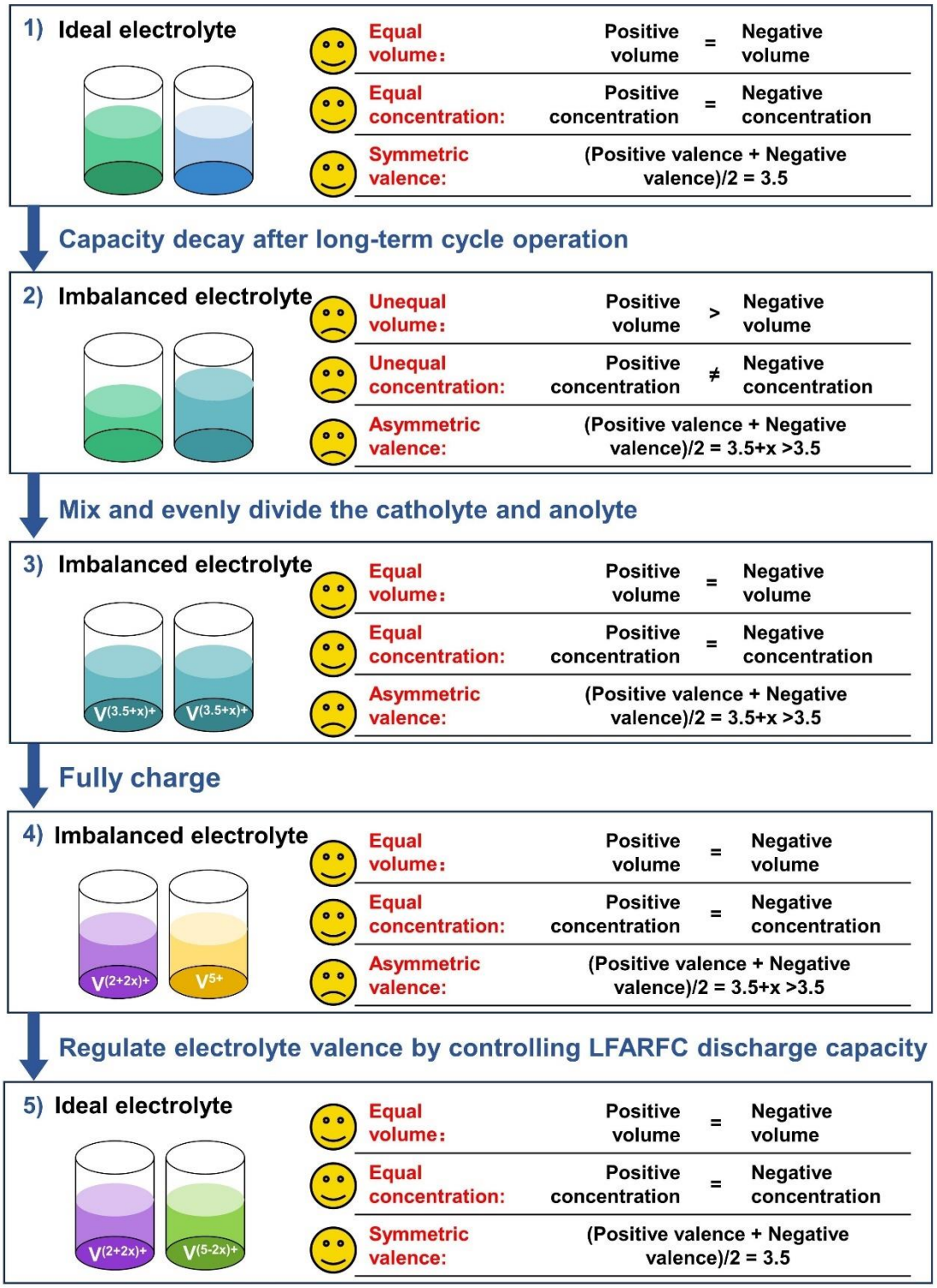

The recovery process in this work is shown in the figure above.

1) To rebalance the volume and concentration of the electrolyte, the positive and

negative electrolytes, after the cycle tests, were mixed in a beaker and circulated back to the battery until the voltage difference of the positive and negative sides was less than 50 mV. Then, the electrolyte in the beaker was evenly divided into two parts and returned to the two tanks of VRFB to eliminate the volume and concentration imbalance. The battery was then pre-charged under the following operation: at 200 mA cm^{-2} to 1.65 V, followed by 100 mA cm^{-2} to 1.65 V, and finally kept the constant voltage at 1.65 V until the charge current was less than 50 mA. The obtained capacity under the above-mentioned charge process is Q (Ah). The change of average valence (x), defined as the difference between the valence of mixed electrolyte to the balanced valence of 3.5, can be calculated according to the following equation:

$$x = 1.5 - \frac{Q * \eta_{CE} * 3600}{F * n} \quad (20)$$

2) Where F is Faraday constant (96485 C/mol), n (mol) is the number of moles of vanadium species on each side, and η_{CE} is the coulombic efficiency of those mentioned above in the fully charging process, it is assumed to be 99.3% according to our previous research.[14]

3) Then, the cathode side of the LFARFC was filled with high-valence V^{5+} electrolyte as catholyte, and the anode side was supplied with 5 M HCOOH as anolyte. The LFARFC was then discharged at a constant current density until the discharge capacity reached a set value. The set values are defined as DC, which can be calculated according to the following equation:

$$DC = 2*x*n*F/3600 = (1.5-\frac{Q * \eta_{CE} * 3600}{F * n})*2*n*F/3600 \text{ (Ah)} \quad (21)$$

4) When discharge capacity reached DC, the valence state of discharged catholyte and the negative electrolyte of the VRFB was close to symmetrical, i.e., the average valence was ~3.5. After that, the discharge catholyte was returned back to the positive tank of the flow battery, and the cycle tests continued. The whole capacity recovery process was completed.

Supplementary Note 10 The details of the polarization measurement test

The polarization curve was measured as follows:

1) The fuel cell was operated in an open circuit state until a stable voltage was reached.
2) The fuel cell was then discharged at an increased current density, which was increased at a step interval of 10.0 mA cm^{-2} until 200 mA cm^{-2}. Next, the step interval became 25 mA cm^{-2} until 600 mA cm^{-2}. The average voltage of the fuel cell was recorded after the step was held for 10 seconds.
3) The polarization curve was determined by connecting the discrete points obtained above.

Figures

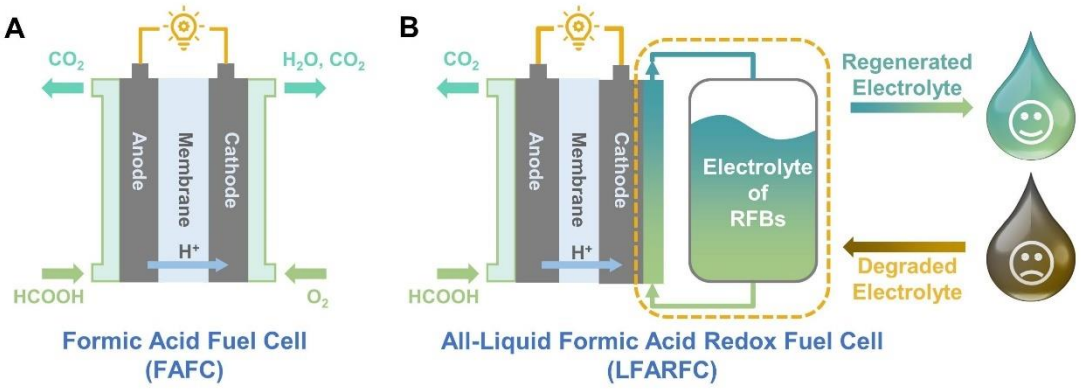

Figure S1. Schematic diagrams of (A) a conventional FAFC and (B) a novel LFARFC.

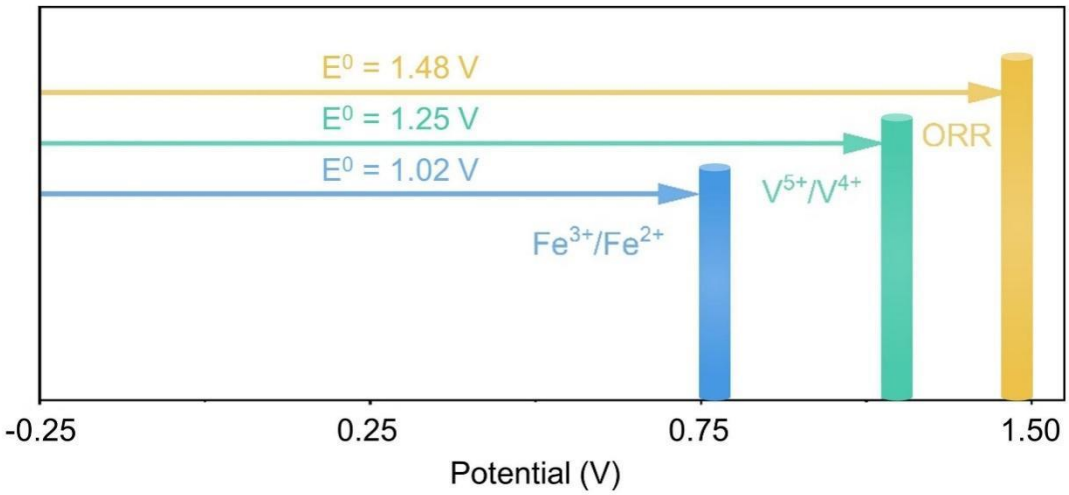

Figure S2. Standard electrochemical potential window between various redox couples and the FAOR.

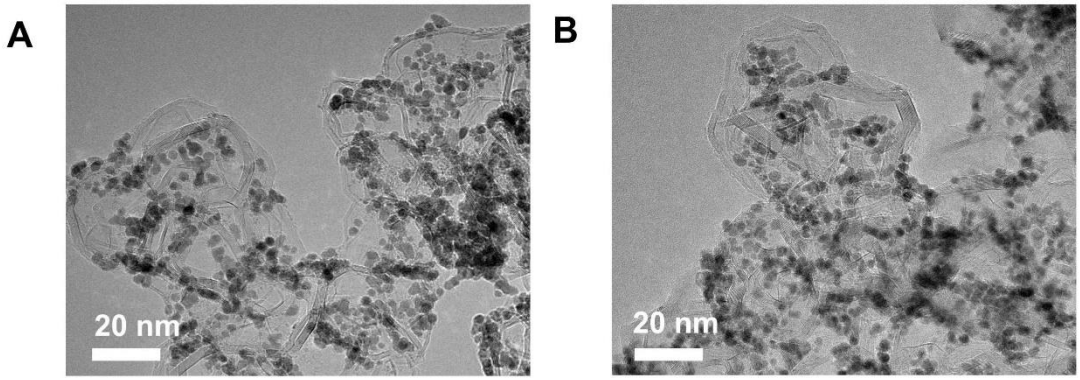

Figure S3. TEM images of (A) Pt/C and (B) Bi-modified Pt/C.

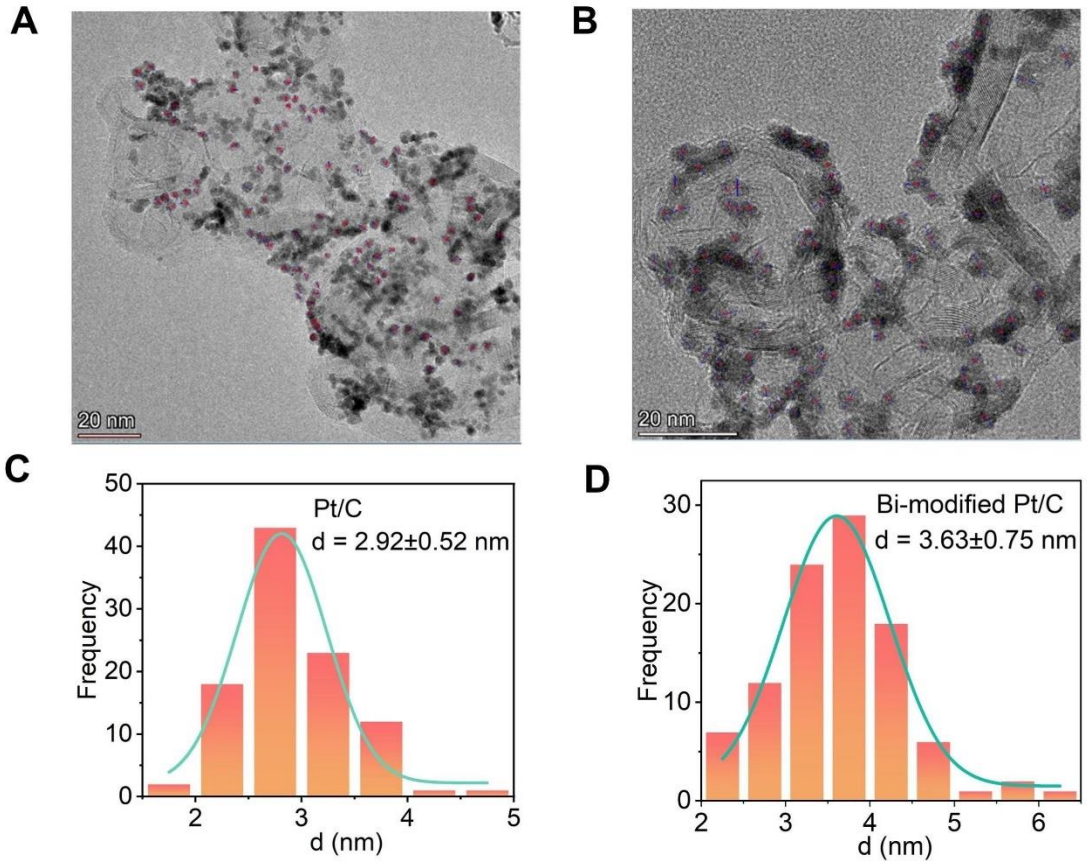

Figure S4. Catalyst particle size analysis. TEM images of (A) Pt/C and (B) Bi-modified Pt/C. Catalyst particle size analysis of (C) Pt/C and (D) Bi-modified Pt/C.

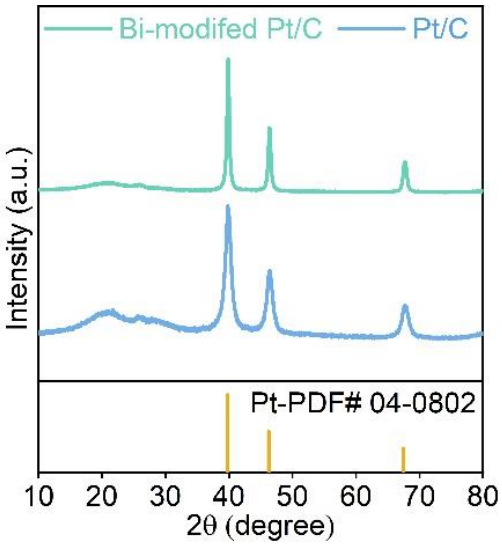

Figure S5. XRD profiles of Pt/C and Bi-modified Pt/C.

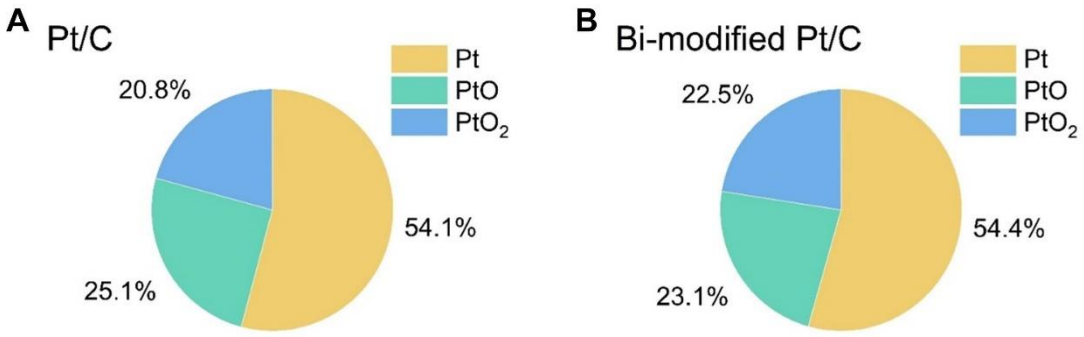

Figure S6. Analysis of the Pt element valence contents in (A) Pt/C and (B) Bi-modified Pt/C

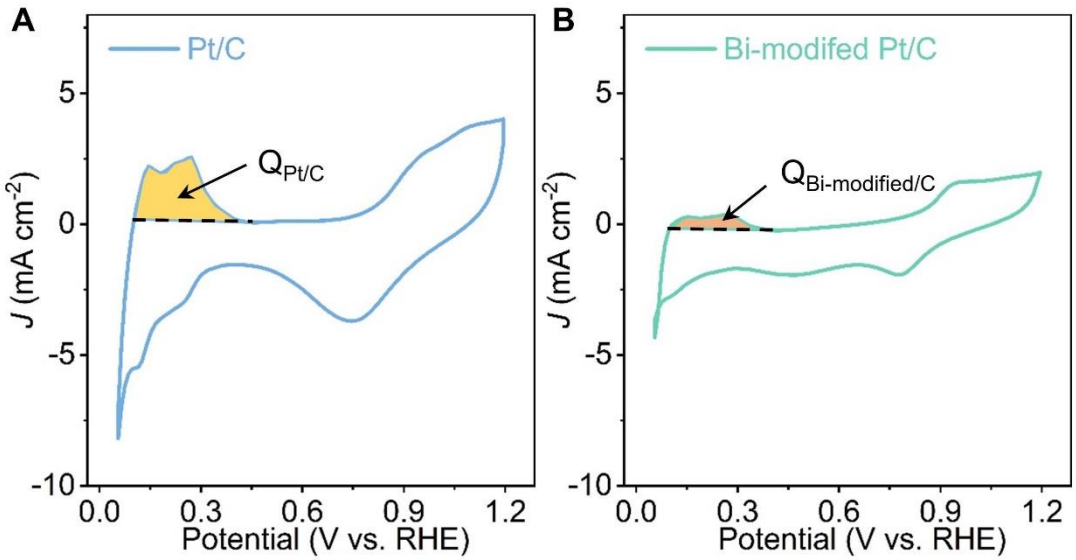

Figure S7. Details of the calculation for Bi coverage in the CV curves of (A) Pt/C and (B) Bi-modified Pt/C.

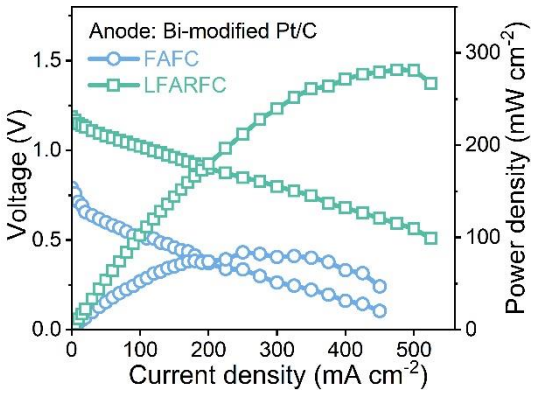

Figure S8. Steady-state polarization and power density curves of FAFC and LFARFC with Bi-modified Pt/C supplied with 5M HCOOH.

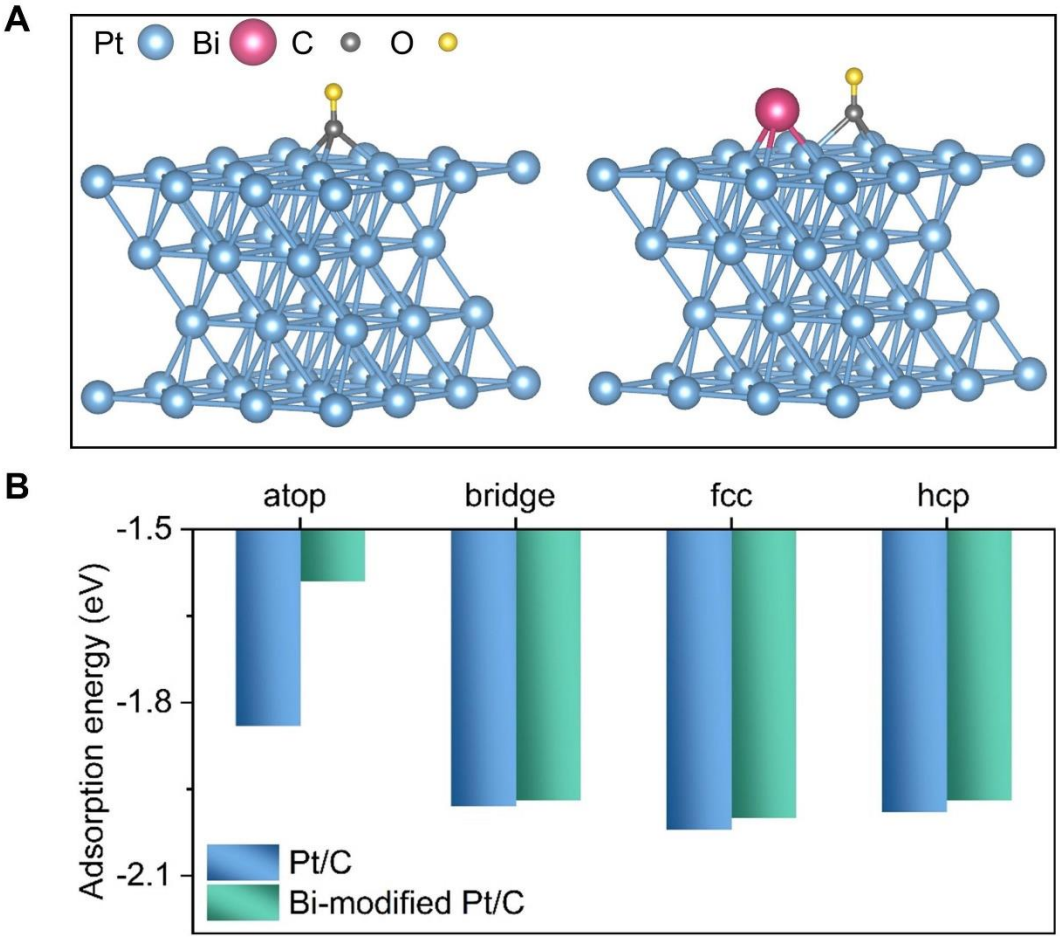

Figure S9. (A) Optimized surface slabs with CO* adsorbed on the surfaces of Pt (left) and Bi-modified Pt (right). (B) CO* adsorption energies at the four adsorption sites on two catalysts.

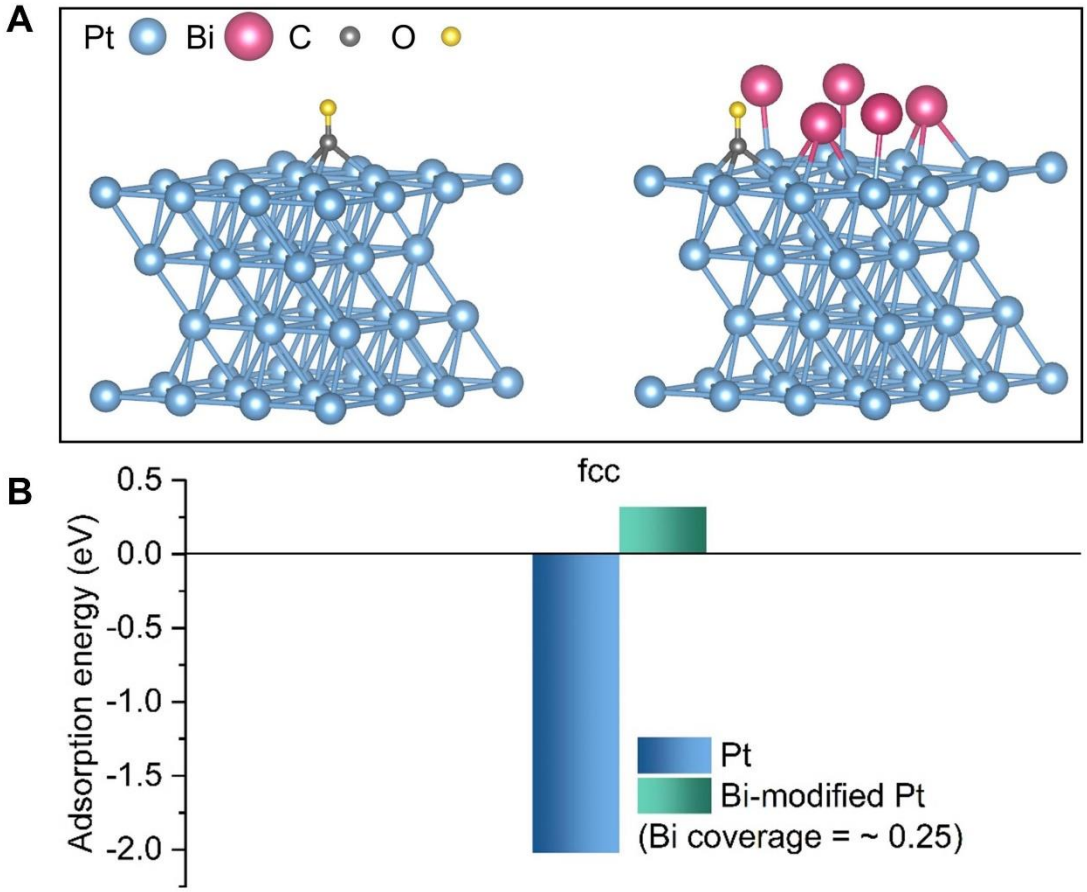

Figure S10. (A) Optimized structures of CO* adsorbed on the surface of Pt (left) and Bi-modified Pt (right, Bi coverage = ~0.25). (B) CO* adsorption energies of two catalysts at the fcc site on two catalysts.

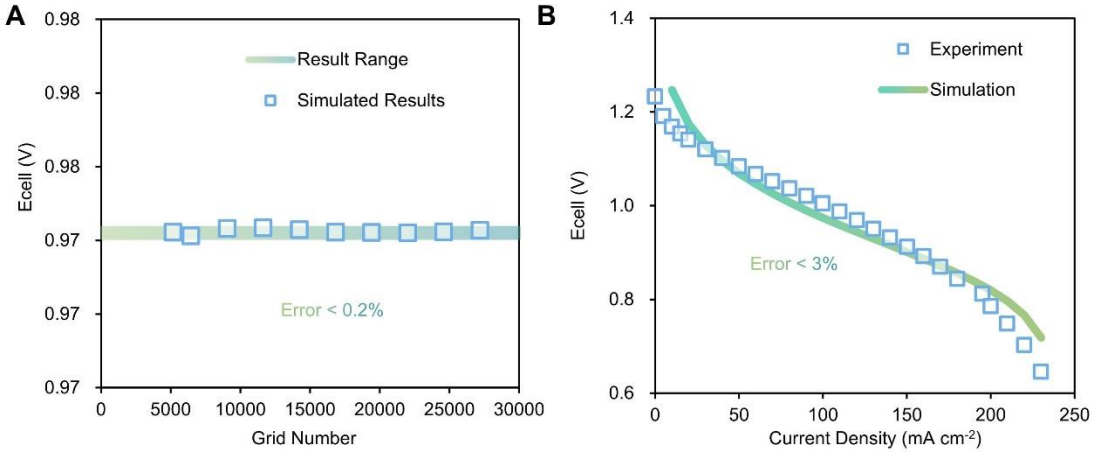

Figure S11. The corresponding (A) grid independence and (B) validation for the model.

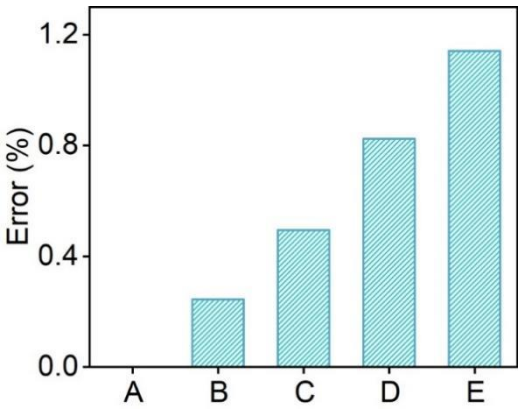

Figure S12. The errors between experimental discharge capacity and theoretical Faraday capacity.

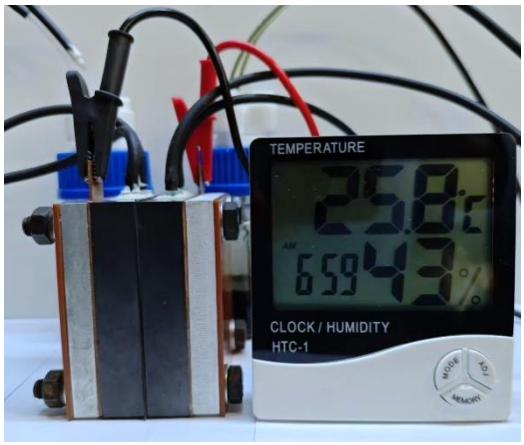

Figure S13. The LFARFC generated voltage that was stabilized at 1.5 V by a voltage booster device and supplied to the electronic temperature hygrometer for operation.

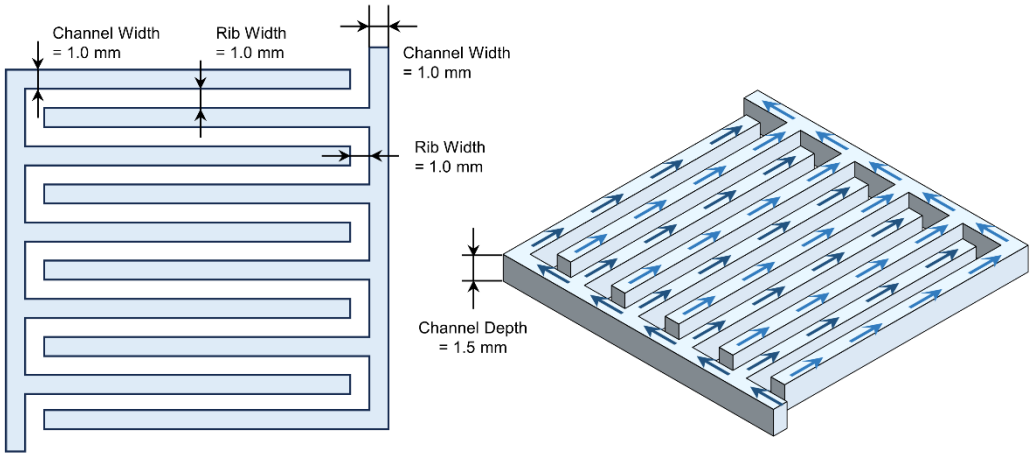

Figure S14. The morphology details of the flow field design.

Tables

Table S1. The previously reported electrocatalysts for formic acid fuel cells.

Reference Number	Anode catalyst	Catalyst loading (mg cm^{-2})	Cathode catalyst	Catalyst loading (mg cm^{-2})	Maximum power density (mW cm^{-2})	Open circuit voltage (V)	Temperature (ºC)
Ref. 1[15]	Pt Black	4.0	Pt Black	7.0	48.8	0.72	60
Ref. 2[16]	Pt Black	4.0	Pt Black	7.0	119	0.65	60
Ref. 3[17]	60% PtRu/C	3.0	Pt Black	5.0	196	0.68	60
Ref. 4[18]	40% Pt-Au/C	4.0	40% Pt/C	4.0	184.8	0.85	60
Ref. 5[1]	40% Bi-modified Pt/C	1.2	Pt Black	3.0	191	0.89	60
Ref. 6[19]	PtPbBi/PtBi	0.5	60% Pt/C	2.0	161.5	0.82	80
Our work	50% Bi-modified Pt/C	1.5	none	0	281.5	1.23	25

Table S2. The numerical details of 3D simulations.

Symbol	Description	Value	Unit
T	Operation temperature	298.15	K
P_{out}	Outlet pressure	0	Pa
Q_{pos}	Positive electrolyte flow rates	40.0	mL min^{-1}
Q_{neg}	Negative electrolyte flow rates	6.0	mL min^{-1}
$\varepsilon_{m,pos}$	Positive electrode porosity	0.81	-
d_0	Positive electrode thickness	0.5	mm
$\varepsilon_{m,neg}$	Negative electrode porosity	0.60 [20]	-
d_0	Negative electrode thickness	0.5	mm
a_{pos}	Positive specific surface area	4.4×10^{4}	m^{-1}
a_{neg}	Negative specific surface area	1.0×10^{3} [13]	m^{-1}
$D_{V^{4+}}$	Diffusion coefficient of V^{4+}	2.40×10^{-10} [21]	$m^2\ s^{-1}$
$D_{V^{5+}}$	Diffusion coefficient of V^{5+}	2.40×10^{-10} [21]	$m^2\ s^{-1}$
D_{FA}	Diffusion coefficient of FA	1.37×10^{-9} [20]	$m^2\ s^{-1}$
ρ_{pos}	Electrolyte density	1.50×10^{3}	kg m^{-3}
μ_{pos}	Electrolyte viscosity	4.93×10^{-3}	Pa s
ρ_{neg}	Electrolyte density	1.03×10^{3} [20]	kg m^{-3}
μ_{neg}	Electrolyte viscosity	0.89×10^{-3} [20]	Pa s
E^0_{pos}	Positive standard potential	1.004 [21]	V
E^0_{neg}	Negative standard potential	-0.250	V

Table S3. The relationships between valence states, state of charge, and cell voltages.

Valence states	4.030	4.025	4.020	4.015	4.010
State of charge	0.030	0.025	0.020	0.015	0.010
Cell voltages	0.743	0.728	0.707	0.675	0.597
Valence states	4.009	4.008	4.007	4.006	4.005
State of charge	0.009	0.008	0.007	0.006	0.005
Cell voltages	0.529	0.512	0.446	0.397	0

Table S4. The capacities and efficiencies of VRFBs within the recovery processes.

Cycle number	0-100	101-200	201-300	301-400	401-500
Starting discharge capacity (mAh)	481.0	474.1	471.0	470.0	469.6
Ending discharge capacity (mAh)	397.1	385.3	380.2	390.1	390.1
Average CE (%)	98.33	98.20	98.19	98.21	98.08
Average EE (%)	82.82	82.52	81.20	80.68	80.56
Average VE (%)	84.23	84.03	82.70	82.15	82.14

Table S5. The comparisons between different capacity recovery methods.

Methods	Recovery Effect	Safety	Cost	Energy/Resource Consumption	Energy Output
Direct Mixing	× Valence √ Volume √ Concentration	High	Low	• Stirring and heat	None
Electrolytic Reduction	√ Valence √ Volume √ Concentration	High	Medium	• External electricity input • Additional electrolyte as oxidants	None
Chemical Reduction		Medium[1]	Medium	• Additional thermal energy input • Chemicals (oxalic acid etc.)	None
V-H_2 cell[2]		Low	High	• Complex storage and transport systems • Chemicals (H_2)	Electricity
Our cell[3]		High	Low	• Chemicals (formic acids)	Electricity

1 It potentially involves significant heat generation.

2 Since H_2 is a flammable and explosive gas, it brings about storage and transport issues, which require high costs for the H_2 and high-pressure tanks. These bring about challenges in the implementation and system integration. Inside the flow-battery energy storage plant, there are many H_2 detection sensors. Once the H_2 concentration inside the plant exceeds the standard, the battery system needs to stop operating and turn on the plant ventilation mode. H_2 tanks are not allowed to be stored inside energy storage power stations, whether at the policy level or in practical applications.

3 Liquid reactants can be stored and used at ambient temperature and normal pressure, facilitating safer and easier storage and transport. Formic acid stands out among liquid reactants for its low toxicity, high safety, and superior energy density, making it an ideal choice for conducting the capacity recovery process. These are the primary evidence for the practicality of our proposed LFARFCs.

Table S6. The chemical compositions and concentrations of the electrolytes.

Experiments	Electrolyte	Volume (mL)	Concentration (M)						
			H_2SO_4	HCOOH	V^{3+}	V^{4+}	V^{5+}	Fe^{2+}	Fe^{3+}
RDE	-	-	0.5	0.5	-	-	-	-	-
FAFC	Anolyte	50	-	5.0	-	-	-	-	-
LFARFC	Anolyte	50	-	5.0	-	-	-	-	-
(Vanadium)	Catholyte	20	3.0	-	-	-	1.0	-	-
LFARFC	Anolyte	50	-	5.0	-	-	-	-	-
(Iron)	Catholyte	20	3.0	-	-	-	-	-	1.0
RFB	Posolyte	20	3.0	-	1.0	1.0	-	-	-
	Negolyte	20	3.0	-	1.0	1.0	-	-	-

Supplemental References

1. M. Choi, C.-Y. Ahn, H. Lee, J. K. Kim, S.-H. Oh, W. Hwang, S. Yang, J. Kim, O.-H. Kim, I. Choi, Y.-E. Sung, Y.-H. Cho, C. K. Rhee and W. Shin, *Applied Catalysis B: Environmental*, 2019, **253**, 187-195.
2. J. F. b. G. Kresse av* *Computational Materials Science*, 1996, **6** 15-50.
3. J. F. b. G. Kresse av* *Computational Materials Science* 1996, **6** 15-50.
4. D. J. G. Kresse, *PHYSICAL REVIEW B*, 1998, **59**.
5. P. E. Blöchl, *Physical Review B*, 1994, **50**, 17953-17979.
6. S. Grimme, J. Antony, S. Ehrlich and H. Krieg, *The Journal of Chemical Physics*, 2010, **132**.
7. S. Grimme, S. Ehrlich and L. Goerigk, *Journal of Computational Chemistry*, 2011, **32**, 1456-1465.
8. N. H. Maslan, M. I. Rosli and M. S. Masdar, *International Journal of Hydrogen Energy*, 2019, **44**, 30627-30635.
9. J. Sun, H. R. Jiang, B. W. Zhang, C. Y. H. Chao and T. S. Zhao, *Applied Energy*, 2020, **259**, 11.
10. J. Newman and N. P. Balsara, *Electrochemical systems*, John Wiley & Sons, 2021.
11. A. A. Shah, M. J. Watt-Smith and F. C. Walsh, *Electrochimica Acta*, 2008, **53**, 8087-8100.
12. X. Shi, X. Huo, O. C. Esan, Z. Pan, L. Yun, L. An and T. S. Zhao, *Energy and AI*, 2023, **14**, 100275.
13. Y. D. Herlambang, J. C. Shyu and S. C. Lee, *Micro & Nano Letters*, 2017, **12**, 860-865.
14. L. Wei, X. Z. Fan, H. R. Jiang, K. Liu, M. C. Wu and T. S. Zhao, *Journal of Power Sources*, 2020, **478**, 228725-228734.
15. S. H. C. Ricea, R.I. Masela,*, P. Waszczukb, A. Wieckowskib, Tom Barnard, *Journal of Power Sources*, 2002, **111** 83–89.
16. C. A. R. Su Haa, Richard I. Masela,*, Andrzej Wieckowskib, *Journal of Power Sources*, 2002 **112** 655–659.
17. M. K. Baizeng Fang, Jong-Sung Yu *, *Applied Catalysis B: Environmental* 2008, **84**, 100–105.
18. C. R. C. Chitturi Venkateswara Rao, and Yasuyuki Ishikawa*, | *J. Phys. Chem. C* 2011, **115**, 21963–21970.
19. X. Hu, Z. Xiao, W. Wang, L. Bu, Z. An, S. Liu, C. W. Pao, C. Zhan, Z. Hu, Z. Yang, Y. Wang and X. Huang, *J Am Chem Soc*, 2023, **145**, 15109-15117.
20. M. Jałowiecka, Z. Bojarska, A. Małolepszy and Ł. Makowski, *Chemical Engineering Journal*, 2023, **451**, 138474.
21. L. Pan, J. Sun, H. Qi, M. Han, L. Chen, J. Xu, L. Wei and T. Zhao, *Journal of Power Sources*, 2023, **570**, 233012.